Bubble Growth in a Two-Dimensional Viscoelastic Foam.

S.L. Everitt, O.G. Harlen *, and H.J. Wilson [1]

Department of Applied Mathematics, University of Leeds, Leeds, LS2 9JT

Abstract

The effects of viscoelasticity on the expansion of gas bubbles arranged in a hexagonal array in a polymeric fluid are investigated. The expansion is driven by the diffusion of a soluble gas from the liquid phase, and the rate of expansion is controlled by a combination of gas diffusion, fluid rheology and surface tension.

In the diffusion limited case, the initial growth rate is slow due to small surface area, whereas at high diffusivity initial growth is rapid and resisted only by background solvent viscosity. In this high Deborah number limit, we see a two stage expansion in which there is an initial rapid expansion up to the size at which the elastic stresses balance the pressure difference. Beyond this time the bubble expansion is controlled by the relaxation of the polymer. We also illustrate how viscoelasticity affects the shape of the bubble.

In addition to a full finite element calculation of the two-dimensional flow, two one-dimensional approximations valid in the limits of small and large gas area fractions are presented. We show that these approximations give accurate predictions of the evolution of the bubble area, but give less accurate predictions of the bubble shape.

Key words: Bubble growth; polymer foams; Oldroyd B; Finite Elements

1 Introduction

Polymeric foams are used in a wide variety of applications due to their low weight, and sound- and shock-absorbing properties. In thermoplastic injection

* To whom correspondence should be addressed.
Email address: oliver@maths.leeds.ac.uk (O.G. Harlen).
[1] Current address: Department of Mathematics, University College London, Gower Street, London WC1E 6BT, UK

moulding a polymeric liquid containing a foaming agent is injected at high pressure into a mould. As the pressure is reduced, bubbles nucleate and expand forming a polymeric foam. The solid-state properties of the resulting foams depend crucially on the size and shape of the polymer interfaces between the bubbles.

Most previous studies of bubble growth have considered the growth of individual spherical gas bubbles in isolation in either Newtonian [1, 4, 2, 10, 21, 22] or viscoelastic fluids [3, 12, 19, 18, 23, 24, 25, 27]. Our earlier paper [9] provides a more detailed review of these 'cell models', where the bubbles are surrounded by a spherical shell of fluid and expand due to the diffusion of gas into the bubble from the surrounding liquid.

In practice bubbles will not remain spherical as the bubble volume fraction increases due to external shear or extensional flows in the polymer melt or because of the presence of neighbouring bubbles. Schwartz and Roy [20] studied a system of closely packed gas bubbles in a gelling liquid using a lubrication approximation for the flow in the films between bubbles. The changing rheology of the fluid is captured using a generalised Newtonian fluid with viscosity dependent on reaction completion. Pozrikidis [17] considered the expansion of two-dimensional bubbles surrounded by a Newtonian liquid, in square and hexagonal arrays, for a specified areal expansion rate.

In this paper we shall study the effects of neighbouring bubbles by considering bubble growth in a symmetric two-dimensional foam of identical gas bubbles. In static foams, the surface tension forces acting on the films separating neighbouring bubbles must be in equilibrium at the Plateau borders where films meet. Thus, in a two-dimensional foam three films joined at a common line must meet at 120^o. Consequently we can construct a symmetric two-dimensional foam from a hexagonal array of cells. We shall compare the solution of the full two-dimensional equations governing bubble growth, using a finite element method, with two one-dimensional approximations. The first approximation is that of circular symmetry which is appropriate for low volume fractions. The second is the opposite extreme: a one-dimensional approximation for bubbles separated by thin liquid windows.

During expansion the fluid between bubbles is subjected to an almost purely extensional flow. For most calculations we shall use the Oldroyd B model as this simple model captures the strong extension hardening found in dilute polymer solutions. However, in order to study the effects of weaker strain hardening we will also consider bubbles expanding in a fluid described by the pom-pom constitutive equations. In this model, which is appropriate for branched polymer melts, there is an upper bound on elastic stress due to branch point withdrawal.

In three dimensions four films meet at angles of 109.47^o. Unlike the two-dimensional case, it is not possible to construct a symmetric three-dimensional foam with planar faces. Although we will not solve the full three-dimensional flow, in view of the geometric differences between two and three dimensional bubble growth we also study two axisymmetric problems that model the stretching of a strut in an open cell foam and the expansion of a circular window between bubbles in a closed cell foam.

Throughout this paper we shall assume that the expansion rate is sufficiently small that fluid inertia may be neglected, bubble growth is isothermal, and the bubble-fluid interface remains in thermodynamic equilibrium.

2 Fluid Model

The stress in a liquid is made up of an isotropic pressure and an extra stress determined by the fluid model,

$$\boldsymbol{\pi} = -p\mathbf{I} + \boldsymbol{\sigma}.$$

With the exception of section 5 the liquid surrounding the bubble is modelled as an Oldroyd B fluid which may be derived from the kinetic theory of a suspension of linear elastic dumbbells [5]. The viscous drag on the molecule is represented by the drag on the dumbbell ends and the entropic force restoring the molecule to an equilibrium configuration is represented by a Hookean spring. Contributions to the extra stress, $\boldsymbol{\sigma}$, come from a Newtonian viscous term with solvent viscosity μ, and a polymer stress with elastic modulus G and configuration tensor $\mathbf{A}$,

$$\boldsymbol{\sigma} = 2\mu\mathbf{E} + G(\mathbf{A} - \mathbf{I}).$$

Here $\mathbf{E} = \frac{1}{2}(\nabla\mathbf{u} + \nabla\mathbf{u}^T)$ where $\mathbf{u}$ is the fluid velocity. The configuration tensor, $\mathbf{A}$, is the ensemble average of the second moment of the dumbbell end-to-end vector and satisfies

$$\overset{\nabla}{\mathbf{A}} = -\frac{1}{\tau}(\mathbf{A} - \mathbf{I}), \tag{1}$$

where $\overset{\nabla}{\mathbf{A}} = \partial\mathbf{A}/\partial t + \mathbf{u}\cdot\nabla\mathbf{A} - (\nabla\mathbf{u})^T\cdot\mathbf{A} - \mathbf{A}\cdot\nabla\mathbf{u}$ is the upper convected derivative. The right hand side represents the relaxation of the polymer stretch back to equilibrium in characteristic time τ.

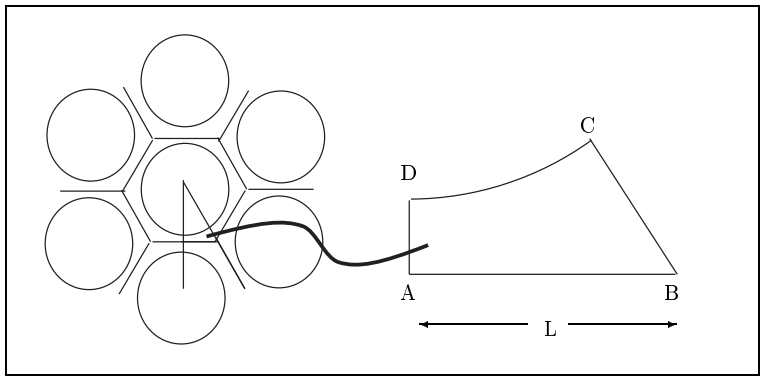

Fig. 1. Diagram showing the two dimensional arrangement of circular bubbles with the computational fluid area enlarged.

3 Bubble Growth in a Two-Dimensional Hexagonal Lattice

We consider identical two-dimensional bubbles arranged in a hexagonal lattice. Due to the symmetry of this system we need only perform calculations on a triangular region making up 1/12 of the hexagonal cell, shown in figure 1. Bubble expansion is driven by the difference in pressure between the gas pressure inside the bubble, $p_g(t)$, and the ambient pressure outside the system, p_a.

Neglecting inertia, the governing equations are conservation of momentum,

$$\nabla \cdot \boldsymbol{\pi} = 0, \tag{2}$$

together with conservation of mass

$$\nabla \cdot \mathbf{u} = 0. \tag{3}$$

By symmetry there are no tangential tractions and no flow through the boundary of the element and so by specifying the rate of increase of the cell length, $\dot{L}$, these equations can be solved for the velocity and pressure within the fluid. In order to find $\dot{L}$ we consider the work done by the fluid stress, bubble gas pressure, ambient pressure and surface tension (S) in changing the bubble area an infinitesimal amount. Since the fluid is incompressible any increase in bubble area produces an equal increase in the size of the system, which does work against the pressure p_a outside the system. This gives the following equation relating the cell expansion rate to the gas pressure difference,

$$\int_{A_f} \boldsymbol{\sigma} : \mathbf{E} \; dA_f = (p_g - p_a)\frac{dA_b}{dt} - S\frac{dC}{dt}. \tag{4}$$

Here, A_f is the fluid area, A_b is the bubble area in the 1/12th sector, and C is the length of the liquid-bubble interface.

The concentration of gas in the liquid, $c(\mathbf{x}, t)$ is governed by the mass transport equation

$$\frac{Dc}{Dt} = \mathcal{D}\nabla^2 c, \tag{5}$$

with diffusivity $\mathcal{D}$. The concentration along the bubble-liquid interface (CD in figure 1) satisfies Henry's law ($c = Hp_g$ where H is Henry's constant), and we impose zero concentration flux along the three remaining boundaries (AB, AD and BC).

Mass conservation across the fluid-bubble interface relates the current gas pressure in the bubble to the amount of gas that has been transferred from the fluid:

$$\frac{d}{dt}\left(\frac{p_g A_b}{RT}\right) = \mathcal{D}\int_C \nabla c \cdot \mathbf{n} dC \tag{6}$$

Here R and T are the gas constant and temperature respectively.

3.1 Non-Dimensional Equations

We scale length with the initial bubble radius, R_0, time with the polymer relaxation time, τ, and the pressure difference, $p_g - p_a$, with $p_{g0} - p_a$, where $p_{g0} = c_0/H$ is the equilibrium pressure at the initial solvent phase concentration. From equation (4) we obtain a dimensionless form of the energy equation

$$\int_{A_f} \boldsymbol{\sigma} : \mathbf{E}\, dA_f = P_g De \frac{dA_b}{dt} - \frac{1}{\Gamma}\frac{dC}{dt}. \tag{7}$$

Here $P_g = \frac{p_g - p_a}{p_{g0} - p_a}$ is the dimensionless gas pressure difference and $\boldsymbol{\sigma}$, $\mathbf{E}$, A_f, A_b and C are now the dimensionless forms of these quantities. Applying these scalings to the Oldroyd B equation (1) results in

$$\overset{\nabla}{\mathbf{A}} = -(\mathbf{A} - \mathbf{I}). \tag{8}$$

Scaling the gas concentration with RT/p_{g0} we obtain the dimensionless form of the gas transport equation

$$\frac{Dc}{Dt} = N\nabla^2 c \tag{9}$$

together with boundary conditions

$$\begin{aligned} c &= \frac{\Phi(p_a + (p_{g0} - p_a)P_g)}{p_{g0}} && \text{at the bubble-liquid interface CD} \\ \mathbf{n} \cdot \nabla c &= 0 && \text{on the boundary AB, AD and BC.} \end{aligned} \tag{10}$$

Integrating the equation for the flux of gas across the bubble surface (6) over time gives

$$(p_a + (p_{g0} - p_a)P_g)A_b = p_{g0}\left(A_{b0} + N\int_t\int_{CD} \nabla c \cdot \mathbf{n}\, dS\, dt\right). \qquad (11)$$

The dimensionless groups arising are summarised in table 1. Equations (7) – (11) together with dimensionless forms of (2) and (3) provide the dimensionless equation set governing bubble growth. Φ is the dimensionless form of the Henry's law constant and is the ratio of the solvent phase to gas phase concentrations. Taking a value for Henry's constant $H = 1.05 \times 10^{-4}\text{molN}^{-1}\text{m}^{-1}$ gives $\Phi = 0.32$ for a temperature of 370K.

Deborah number	$De = \frac{(p_{g0}-p_a)\tau}{(\mu+G\tau)}$	ratio of the bubble growth rate at the zero-shear-rate viscosity to the relaxation rate of the polymer
viscosity ratio	$\beta = \frac{G\tau}{\mu+G\tau}$	proportion of zero-shear-rate viscosity contributed by the polymer
capillary number	$\Gamma = \frac{R_0(\mu+G\tau)}{S\tau}$	ratio of viscous forces (based on zero-shear-rate viscosity) to surface tension
gas solubility	$\Phi = RTH$	ratio of solvent phase to gas phase concentration
time scale ratio	$N = \frac{\mathcal{D}\tau}{R_0^2} = \frac{\tau}{T_d}$	ratio of the polymer relaxation time, τ, to gas diffusion time, T_d

Table 1
Dimensionless groups arising in the non-dimensional formulation of the equations governing bubble growth.

3.2 Finite Element Solution

The presence of the free surface, and the absence of flow through the boundaries, makes the flow calculation well suited to Lagrangian computational methods. Consequently we shall use the split Eulerian-Lagrangian finite element method developed by Harlen *et al.* [13]. The equations are solved on triangular finite elements that move and deform with the fluid.

Following the approach taken in reference [13] the polymeric stress is split into a 'viscous' part equivalent to the stress exerted by the dumbbell in order to

retain its current length and an 'elastic' part caused by changes in the length of the dumbbell. Using equation (8) we may write the polymer contribution to the stress

$$\mathbf{A} - \mathbf{I} = \mathbf{A} \cdot \mathbf{E} + \mathbf{E} \cdot \mathbf{A} - \overset{\circ}{\mathbf{A}}$$

where $\overset{\circ}{\mathbf{A}} = \partial \mathbf{A}/\partial t + \mathbf{u} \cdot \nabla \mathbf{A} - \mathbf{A} \cdot \mathbf{\Omega} + \mathbf{\Omega} \cdot \mathbf{A}$ is the corotational derivative and $\mathbf{\Omega} = \frac{1}{2}(\nabla \mathbf{u} - \nabla \mathbf{u}^T)$ is the vorticity tensor. Thus the extra stress can be written in the form

$$\sigma_{ij} = \mu_{ijkl} E_{kl} - \beta \overset{\circ}{A}_{ij}.$$

where $\mu_{ijkl} = (\delta_{ik} + \beta A_{ik})\delta_{jl} + \delta_{ik}(\delta_{jl} + \beta A_{jl})$ is an effective viscosity. This allows the momentum equation to be rewritten as

$$-\nabla p + \nabla \cdot (\boldsymbol{\mu} : \mathbf{E}) = \beta \nabla \cdot \overset{\circ}{\mathbf{A}}. \tag{12}$$

At each time step, equation (12) together with conservation of mass are solved via the finite element method for current values of $\mathbf{A}$ and $\overset{\circ}{\mathbf{A}}$ and an estimate for the expansion rate $\dot{L}$. By separating the terms in equation (7) into those that are linear and quadratic in the velocity we can obtain a new estimate for $\dot{L}$. The velocity is then recalculated and the value of $\dot{L}$ is further refined by linear interpolation. In practice at most three iterations are required to find the correct value of $\dot{L}$.

Once the velocity field has been found, the positions of the nodes of the finite elements are updated. The configuration tensor $\mathbf{A}$ is then found by integrating equation (8) in the frame of the deforming element, where the upper convected derivative becomes $\frac{d\mathbf{A}}{dt}$. The solution for $\mathbf{A}$ is thereby reduced to a first-order ordinary differential equation.

The gas transport equation (9) is solved using the same finite elements used to solve the momentum equation and makes use of the Lagrangian nature of the grid to remove the advection term. We use a backward Euler scheme to discretize time; the Laplacian is discretized using the standard Galerkin method and the resulting linear system is solved by a preconditioned conjugate gradient method. The value of the bubble gas pressure is calculated from the flux of gas across the bubble-liquid interface using equation (11).

The calculations were performed using grids with approximately 1000 elements and a timestep of $10^{-3}L/\dot{L}$. Spatial accuracy was checked by comparing calculated values for $\mathbf{A}$, $\mathbf{u}$, $\dot{L}$ and bubble area for one set of parameter values with those obtained using a finer grid with approximately 4000 elements and were found to be within a relative error of 0.5%. A separate check of temporal accuracy using a timestep of $5 \times 10^{-4}L/\dot{L}$ found relative errors in $\mathbf{A}$ of at most 1% and smaller errors in other quantities.

3.3 Circular Bubbles

When the bubble area fraction is small we might expect bubbles to remain circular during the expansion, thus we can consider a simplified model where circular bubbles are surrounded by a circular liquid layer.

In cylindrical polar coordinates the liquid pressure, p, and stresses, σ_{rr} and $\sigma_{\theta\theta}$, are assumed to depend on r and time t only. Neglecting inertia, the radial component of the momentum equation, $\nabla \cdot \boldsymbol{\sigma} = 0$, gives

$$\frac{\partial p}{\partial r} = \frac{(\sigma_{rr} - \sigma_{\theta\theta})}{r} + \frac{\partial \sigma_{rr}}{\partial r}. \tag{13}$$

Since the fluid area is conserved we transform from a radial coordinate r to a Lagrangian area coordinate x such that $r^2 = a_b + x$. Here, πa_b is the bubble area and πx is the general fluid area so that $x = X$ is the Lagrangian position of the outer edge of the liquid layer. At the boundaries $x = 0$ and $x = X$

$$-p(a_b) + \sigma_{rr}(a_b) = -p_g + \frac{S}{a_b^{\frac{1}{2}}} \quad \text{(inner surface boundary condition)}$$
$$-p(X + a_b) + \sigma_{rr}(X + a_b) = -p_a \quad \text{(outer surface boundary condition)}$$

where S is the surface tension at the bubble surface. Integrating equation (13) for the Oldroyd B fluid gives

$$\dot{a_b}\left[\frac{1}{a_b} - \frac{1}{X + a_b}\right] = P_g De + \frac{1}{2}\beta \int_0^X \frac{A_{rr} - A_{\theta\theta}}{x + a_b} dx - \frac{1}{\Gamma}\frac{1}{a_b^{\frac{1}{2}}}. \tag{14}$$

Due to the coordinate transformation, the evolution of A_{rr} and $A_{\theta\theta}$, given by equation (1), can be followed in the Lagrangian frame:

$$\frac{\partial A_{rr}}{\partial t} = -\frac{\dot{a_b}}{(x + a_b)} A_{rr} - (A_{rr} - 1), \tag{15}$$

and

$$\frac{\partial (A_{rr} - A_{\theta\theta})}{\partial t} = \frac{\dot{a_b}}{(x + a_b)} \left[(A_{rr} - A_{\theta\theta}) - 2A_{rr}\right] - (A_{rr} - A_{\theta\theta}). \tag{16}$$

Initially $A_{rr} = 1$ and $A_{rr} - A_{\theta\theta} = 0$ everywhere.

We introduce a concentration potential $\psi(x, t)$ so that $\partial\psi/\partial x = c - c_0$ to aid in the numerical solution of the gas transport equation (5) [1, 4, 9]. The diffusion equation then becomes

$$\frac{\partial \psi}{\partial t} = 4N(x + a_b)\frac{\partial^2 \psi}{\partial x^2}, \tag{17}$$

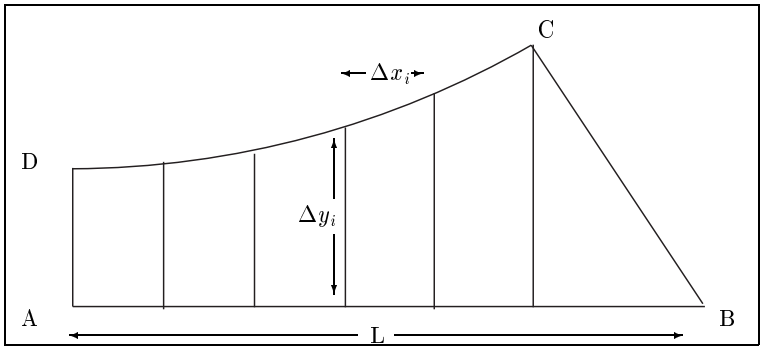

Fig. 2. Sketch of the subdivision of the fluid region in the thin film approximation.

with $\partial\psi/\partial x = \Phi(p_{g0} - p_{a_b})(P_g - 1)/p_{g0}$ at the bubble surface, satisfying Henry's law. We impose the condition of no mass transport of gas through the outer edge of the fluid layer, $x = X$ so that from equation (17) $\psi(X,t) = \psi(X,0)$.

Finally the gas pressure is given by

$$(p_a + (p_{g0} - p_a)P_g)a_b = p_{g0}(1 + \psi(0,t)), \tag{18}$$

where we have set $\psi(0,0) = 0$. Hence a uniform initial gas concentration is given by

$$\psi(x,0) = \Phi\frac{(p_{g0} - p_a)}{p_{g0}}x.$$

3.4 Thin Film Approximation

In the opposite limit where the bubbles are separated by thin films, we can obtain a second one-dimensional approximation. Since there is no traction along either the bubble surface or the x-axis, the flow in the liquid region is approximately an extensional flow in the x-direction. Thus, when the fluid layer is thin, the velocity gradient and the polymer stress will be approximately uniform over the thickness of the fluid layer and we can construct a one dimensional thin film model analogous to those used to model spin lines [11, 14].

We divide the fluid region into n trapezoidal elements and a triangle as shown in figure 2, where Δx_i is the width of element i and Δy_i is the height of the left-hand edge.

Integrating the momentum equation (2) over element i and applying the divergence theorem we obtain

$$\int_{C_i} \boldsymbol{\pi} \cdot \mathbf{n}\, dC_i = 0$$

where C_i is the boundary of element i. We assume that, since the fluid layer is thin, the stress components, π_{xx} and π_{yy}, are independent of y. Thus the integrals along the vertical edges are

$$-(-p+\sigma_{xx})_i \Delta y_i \ \hat{\mathbf{x}} \qquad \text{and} \qquad (-p+\sigma_{xx})_{i+1} \Delta y_{i+1} \ \hat{\mathbf{x}}.$$

The contribution from the gas-liquid interface is obtained by using the boundary condition

$$\boldsymbol{\pi} \cdot \mathbf{n} = (-p_g + S\kappa)\mathbf{n}$$

where the curvature, κ, is given by

$$\kappa = \frac{\Delta y''}{(1+\Delta y'^2)^{3/2}} = -\frac{1}{\Delta y'} \frac{d}{dx} \left(\frac{1}{(1+\Delta y'^2)^{1/2}} \right).$$

Thus the contribution from the gas-liquid interface becomes

$$-\left(-p_g(\Delta y_{i+1} - \Delta y_i) - \frac{S}{(1+\Delta y_{i+1}'^2)^{1/2}} + \frac{S}{(1+\Delta y_i'^2)^{1/2}} \right) \hat{\mathbf{x}} + \int (-p_g + S\kappa)\, dx \hat{\mathbf{y}}.$$

Finally, the contribution from the symmetry line along the bottom of element i is

$$\int (-p+\sigma_{yy})\hat{\mathbf{y}} \ dx.$$

Contributions from each of the four integrals are then combined. Balancing the y components gives an expression for the pressure in the fluid,

$$\sigma_{yy} = -(p_g - p) + S\kappa. \tag{19}$$

The x components relate the stress and fluid pressure at the left hand end of each element to that at its right hand end; using equation (19) to eliminate the fluid pressure we obtain the non-dimensional equation for the force balance on each element,

$$\left(\sigma_{xx} - \sigma_{yy}\right)_{i+1} \Delta y_{i+1} = \left(\sigma_{xx} - \sigma_{yy}\right)_i \Delta y_i - \frac{1}{\Gamma} \left(\kappa_{i+1} \Delta y_{i+1} - \kappa_i \Delta y_i + \frac{1}{\sqrt{1+\Delta y_{i+1}'^2}} - \frac{1}{\sqrt{1+\Delta y_i'^2}} \right). \tag{20}$$

To obtain an expression for the expansion rate, $\dot{L}$, we again consider the work done in expanding the bubble an infinitesimal amount as in equation (7). For our discretised system we obtain

$$\sum_i \boldsymbol{\sigma} : \mathbf{E} A_i = P_g De \frac{dA_b}{dt} - \frac{1}{\Gamma} \sum_i \frac{dC_i}{dt}$$

where $A_i = \frac{1}{2}(\Delta y_{i+1} + \Delta y_i)\Delta x_i$ is the area i and $C_i = \sqrt{\Delta x_i^2 + (\Delta y_{i+1} - \Delta y_i)^2}$ the length of the bubble-liquid interface of element i. Thus

$$\frac{1}{2}\sum_i (\Psi_{i+1} + \Psi_i)\frac{d\Delta x_i}{dt} = \sqrt{3}P_g DeL\frac{dL}{dt} - \frac{1}{\Gamma}\sum_i \frac{dC_i}{dt} \tag{21}$$

where we have defined $\Psi = (\sigma_{xx} - \sigma_{yy})\Delta y$. For the Oldroyd B fluid

$$\Psi = \left(-\frac{4}{\Delta y}\frac{d\Delta y}{dt} + \beta(A_{xx} - A_{yy})\right)\Delta y, \tag{22}$$

while from equation (8), the evolution of the elastic stresses is given by

$$\frac{dA_{xx}}{dt} = -\frac{2}{\Delta y}\frac{d\Delta y}{dt}A_{xx} - (A_{xx} - 1), \tag{23}$$

$$\frac{dA_{yy}}{dt} = \frac{2}{\Delta y}\frac{d\Delta y}{dt}A_{yy} - (A_{yy} - 1). \tag{24}$$

We shall assume that gas diffusion is effectively instantaneous so that gas concentration is uniform throughout the fluid. This will be valid provided that time for the gas to diffuse across the length BC is short compared to the bubble expansion time ($N \gg De$).

By Henry's law the amount of gas that has diffused into the bubble is

$$\Phi\frac{(p_{g0} - p_a)}{p_{g0}}(1 - P_g)A_f,$$

and so from conservation of mass (11)

$$(p_{g0} - p_a)P_g = p_{g0}\left(\frac{\frac{\sqrt{3}}{2}{L_0}^2 - A_f + \Phi A_f}{\frac{\sqrt{3}}{2}L^2 - A_f + \Phi A_f}\right) - p_a. \tag{25}$$

Finally, conservation of fluid area requires that

$$(\Delta y_{i+1} + \Delta y_i)\frac{d\Delta x_i}{dt} = -\left(\frac{d\Delta y_{i+1}}{dt} + \frac{d\Delta y_i}{dt}\right)\Delta x_i. \tag{26}$$

Equations (20)–(26) govern the deformation of the region under consideration. As with the calculation of the full finite element problem, we separate the solution of the force balance and conservation of mass equations from the evolution of the constitutive equation. Using an initial estimate for the expansion rate at the midpoint of the window we calculate values of Δy_i from equation (20) using the Crank-Nicolson method to evaluate the curvature terms, we then adjust the expansion rate via a secant method to satisfy equation (21) using values of $d\Delta x/dt$ obtained from equation (26). In order to conserve the area

of the whole of the fluid region the change in area of the triangle is calculated and distributed equally between the trapezia allowing their lengths to be adjusted. Once the Δy and Δx have been updated the bubble gas pressure is calculated by equation (25) and the stresses are updated by evolving equation (23).

4 Results and Discussion

We assume that the bubbles are sufficiently far from each other initially that they are circular and that the polymers are unstretched. We do not attempt to model nucleation and the very early stages of bubble growth so the value of the initial bubble radius, R_0, is not the value at nucleation but that defined by the gas pressure being at p_{g0}.

For an isolated spherical bubble, the only effect of surface tension is to modify the pressure difference between the gas and the fluid and, hence, the final bubble size. Consequently the expansion of an isolated bubble is governed by three timescales [9]: a polymer relaxation time, τ; a viscous growth time, τ/De; and a gas diffusion time, τ/N. However, bubbles expanding in a hexagonal lattice do not necessarily remain circular so that there is an additional timescale controlling the expansion: the time for surface tension to restore circular bubbles. At high capillary number the surface tension timescale is much longer than the bubble expansion timescale and so the bubbles expand to some quasi-equilibrium shape before relaxing to either a circular shape or, if the gas area fraction is greater than the maximum of $\pi/(2\sqrt{3}) = 0.907$, to circular arcs connected to thin, 'black', films.

We first consider the case when the rate of gas diffusion is faster than the expansion rate ($N \gg De$). In this regime we would expect to see the effects of viscoelasticity as the expansion rate is controlled by the fluid rheology. If gas diffusion is instantaneous then the gas concentration throughout the fluid region will be equal to

$$c = \Phi \frac{p_a + (p_{g0} - p_a)P_g}{p_{g0}}.$$

When the expansion is rapid compared to the polymer relaxation time (high Deborah number) it can be divided into two regions. Initially we see a period of rapid expansion as the resistance to expansion is from the solvent alone. In figure 3 we compare the expansion of a bubble in a viscoelastic liquid and Newtonian liquid of the same zero-shear-rate viscosity. In these simulations the initial bubble area fraction is $\phi_0 = 0.630$ and $p_{g0} = 10p_a$, so that in the absence of surface tension the dimensionless bubble area grows from π

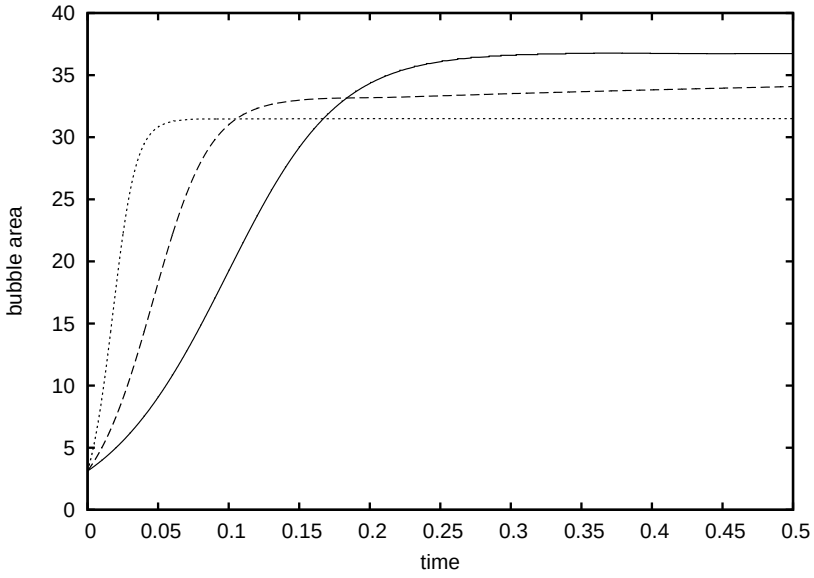

Fig. 3. The effect of the viscosity ratio β on the evolution of the bubble area for $De = 10$, $p_{g0} = 10p_a$ and $\phi_0 = 0.630$: solid line: $\beta = 0$; dashed line: $\beta = 0.5$; dotted line: $\beta = 0.8$.

to final value of 36.73 equivalent to a bubble area fraction of 0.952. Since the solvent contribution to the zero-shear-rate viscosity is smaller by a factor $1-\beta$ in the viscoelastic liquid the early expansion is more rapid for increasing β. The normal stress difference increases during this phase until it balances the gas pressure difference. Beyond this time further expansion occurs, as the polymer stress relaxes, at the polymer relaxation rate. This two-phase expansion behaviour was seen in our earlier calculations for spherical bubbles [9].

Comparing the shape of the liquid-bubble interface at equal bubble areas we find that bubbles in viscoelastic liquids have a flatter thicker window than in a Newtonian fluid. Initially the extension rates are highest in the middle of the window, producing higher polymer extensions that resist further extension of this region. Indeed, for high Deborah number expansions we see an elastic recoil in which fluid is pulled back towards the middle region so that the window thickens there eventhough the bubble is still expanding. This elastic recoil can be seen in figure 4 where we show the evolution of the thickness of the narrow end of the liquid region (AD in figure 1). As the fraction, β, of polymer to solvent contributions to the zero-shear-rate viscosity is increased the magnitude of the 'bounce' increases and the minimum thickness occurs earlier.

This phenomenon can be explained by considering the force balance within the thin film approximation. In the limit of zero surface tension, $\Psi = (\sigma_{xx} - \sigma_{yy})\Delta y$ is independent of x, from equation (20). Consequently, for the Oldroyd B

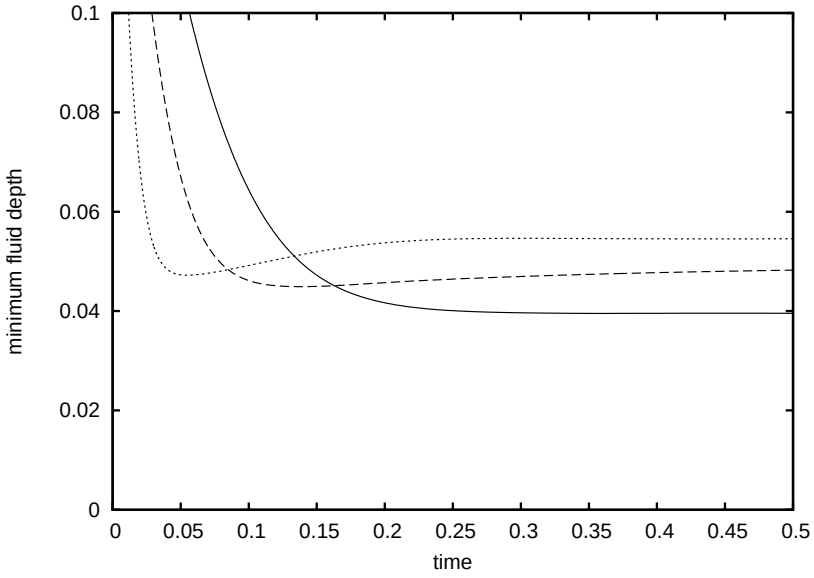

Fig. 4. The evolution of the minimum fluid depth for $De = 10$, $p_{g0} = 10p_a$ and $\phi_0 = 0.630$. Solid line: $\beta = 0$; dashed line: $\beta = 0.5$; dotted line: $\beta = 0.8$.

model, equation (22) we have

$$-4\frac{d\Delta y}{dt} + \beta(A_{xx} - A_{yy})\Delta y = F(t) \tag{27}$$

where $F(t) = \sqrt{3}DeLP_g$ is independent of x. Thus for high Deborah numbers and small t, when $\beta(A_{xx} - A_{yy})\Delta y \ll F(t)$, the absolute change in Δy is approximately equal for all x, and so the largest strain occurs at the thinnest part of the window. For large values of A_{xx}, the polymeric stress difference is given approximately, from equation (23), by

$$\beta(A_{xx} - A_{yy}) \simeq \beta\left(\frac{\Delta y_0}{\Delta y}\right)^2 e^{-t}. \tag{28}$$

The polymeric stress difference grows rapidly as Δy decreases until at $\Delta y \simeq \beta(\Delta y_0)^2 e^{-t}/F(t)$ the elastic stress balances the pressure difference driving the expansion. In the case of an isolated bubble [9] symmetry requires that this balance is achieved simultaneously at all points on the bubble surface, however for bubbles expanding in an array this balance occurs first at the minimum thickness. Since $F(t)$ is controlled by the overall expansion of the window, it continues to decreases faster than the polymer relaxation rate, and so in order to maintain equality in equation (27) Δy must increase in regions of the window where the elastic balance has been achieved. Only once the stress balance is achieved across the window is the expansion rate slowed to the polymer relaxation rate, beyond which time the minimum thickness decreases again.

Figure 5 shows snapshots of the polymer stress distribution in the liquid during

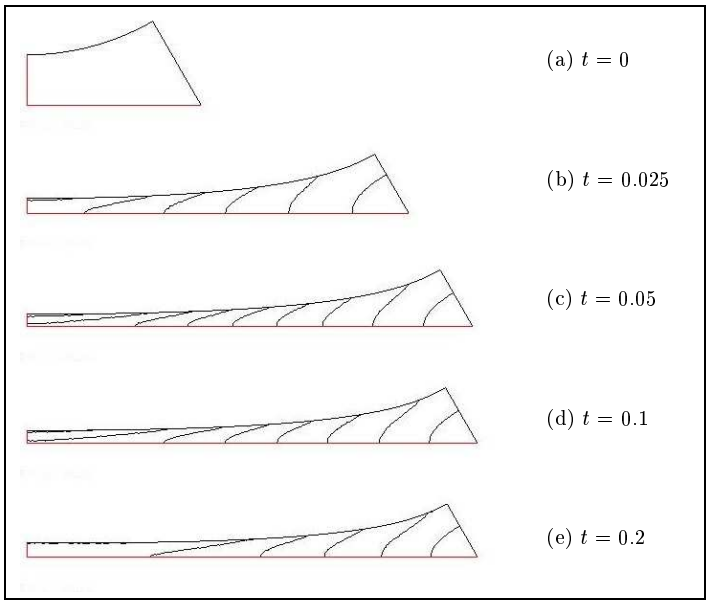

Fig. 5. Contour plots of the difference in the eigenvalues of $\mathbf{A}$ at: (a) $t = 0$; (b) $t = 0.0255$; (c) $t = 0.05$; (d) $t = 0.1$; and (e) $t = 0.2$, for $De = 10$, $\beta = 0.8$, $p_{g0} = 10p_a$ and $\phi_0 = 0.630$. Contour interval is equal to 2 and the stress difference is zero at point C.

the expansion, plotted as the difference in the eigenvalues of $\mathbf{A}$. Initially, (a), there is no polymer stress while at time $t = 0.05$ (just before the turning point in the minimum fluid depth) (b) shows the middle of the window becoming stretched. Pictures (c) and (d) show the stress during the relaxation phase where recoil is seen.

At small capillary numbers surface tension affects the bubble growth in two ways: it relaxes towards a circular bubble; and it reduces the final bubble size by maintaining a higher bubble gas pressure. We do not attempt to model window breakage and the final, surface tension driven, phase of the expansion here. In the absence of intermolecular forces windows will not break in finite time but tend to circular arcs connected by very thin, 'black', films. The rupture of thin films due to Van Der Waals forces is considered by Vaynblat, Lister and Witelski [26] and Zhang and Lister [28] who include depth dependent, inter-molecular, forces.

In figure 6 we compare the evolution of the length of the edge BC between Newtonian and viscoelastic liquids of the same zero-shear-rate viscosity for three different values of the capillary number, $\Gamma = 0.2$, 1 and 5. In the Newtonian case the bubble expands in area up to a time of around $t = 0.3$. After this time surface tension acts to restore circular arcs by drawing fluid towards the corner region. In a viscoelastic fluid at large Deborah number the bubble initially expands rapidly until a stress balance is achieved betwen the bubble

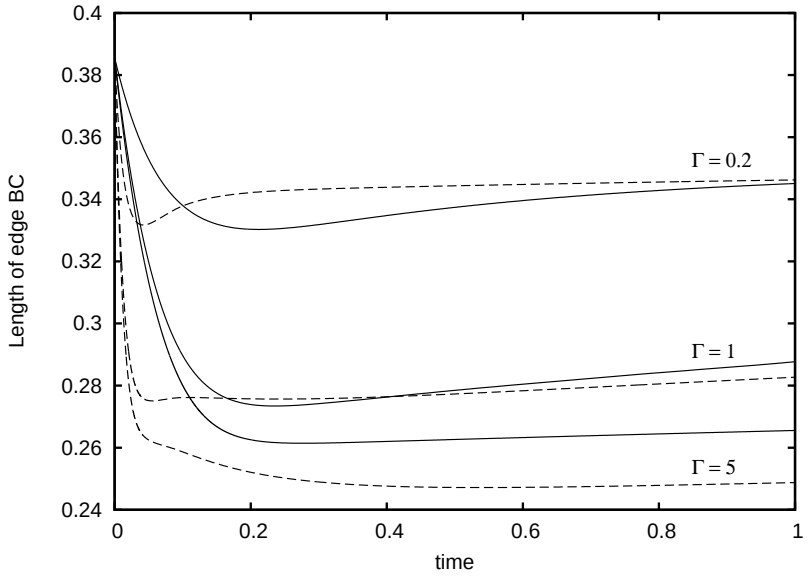

Fig. 6. Comparison of the evolution of the length of the edge BC between a Newtonian liquid and viscoelastic liquid for $De = 10$, $p_{g0} = 10p_a$, $\phi_0 = 0.630$ and $\Gamma = 0.2$, 1 and 5. Solid lines: Newtonian liquid $\beta = 0$, dashed lines: viscoelastic liquid, $\beta = 0.8$.

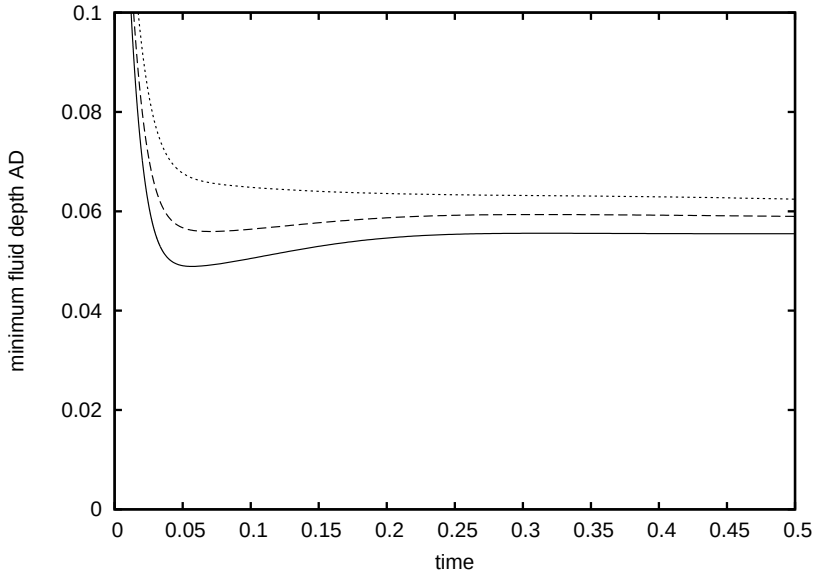

Fig. 7. Evolution of the minimum fluid depth (AD) for $De = 10$, $p_{g0} = 10p_a$, $\phi_0 = 0.630$ and $\beta = 0.8$: solid line: $\Gamma = 5$; dashed line: $\Gamma = 1$; dotted line $\Gamma = 0.5$.

pressure and the elastic stress difference at $t = 0.05$. After this time there is a competition between viscoelasticity and surface tension, with surface tension trying to draw fluid into the corners while viscoelasticity tries to pull fluid in from the corners. At small capillary numbers ($\Gamma = 0.2$) surface tension dominates over viscoelasticity. The edge length CD reaches a minimum at the end of the bubble expansion phase and then grows again as the shape relaxes to a circle. Surface tension reduces the final bubble size which reduces

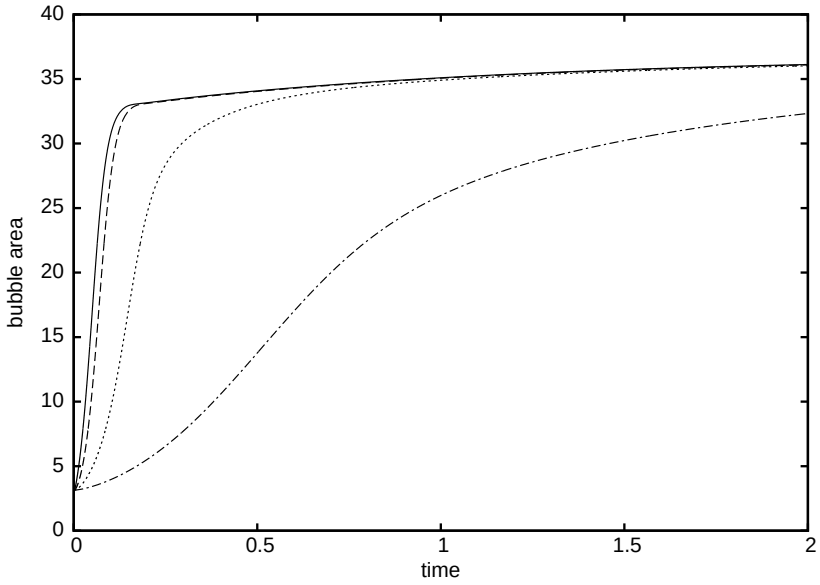

Fig. 8. The effect of gas diffusivity on bubble growth for $De = 10$, $p_{g0} = 10p_a$, $\phi_0 = 0.630$, $\beta = 0.5$ and $1/\Gamma = 0$: solid line, $N = 10$; dashed line, $N = 1$; dotted line, $N = 0.1$; dash-dot line, $N = 0.01$

the strain available for stretching the polymers. The viscoelastic stresses are smaller and the differences between the Newtonian and viscoelatic case are mostly due to change in solvent viscosity. For intermediate capillary numbers ($\Gamma = 1$) the bubbles develop more of a hexagonal asymmetry as they expand so that there is larger recovery of the edge length in relaxing to a circular bubble. This relaxation is noticably slower for the viscoelastic fluid because the elastic stresses resist the effects of surface tension by pulling fluid away from this region. At large capillary number ($\Gamma = 5$) the viscoelastic stresses dominate initially so that fluid is drawn out of the corners as minimum thickness increases. However, ultimately surface tension will restore circular arcs once the polymer stresses have relaxed. This competition between viscoelastic and surface tension forces is also seen in thickness of the minimum depth AD. In figure 7 we see that the magnitude of the 'bounce' at $t = 0.05$ is much smaller for $\Gamma = 1$ than for $\Gamma = 5$ and that the thickness then decreases again as surface tension pulls fluid into the corner region. For $\Gamma = 0.5$ and lower, the minimum is lost altogether.

In the limit of infinite gas diffusivity the initial bubble pressure is set by Henry's law to be p_{g0}. However, at finite gas diffusivity a number of different choices have been suggested [10]. Following [10] we choose the initial gas pressure equal to dynamic equilibrium bubble pressure, $P_g = 1/(De\Gamma)$, so that the bubble only expands due to diffusion of gas into the bubble. The initial gas concentration, c_0, in the liquid is chosen to be

$$c_0 = \frac{p_{g0}[\Phi(1-\phi_0)+\phi_0] - \phi_0(p_a + \frac{p_{g0}-p_a}{De\Gamma})}{p_{g0}(1-\phi_0)},$$

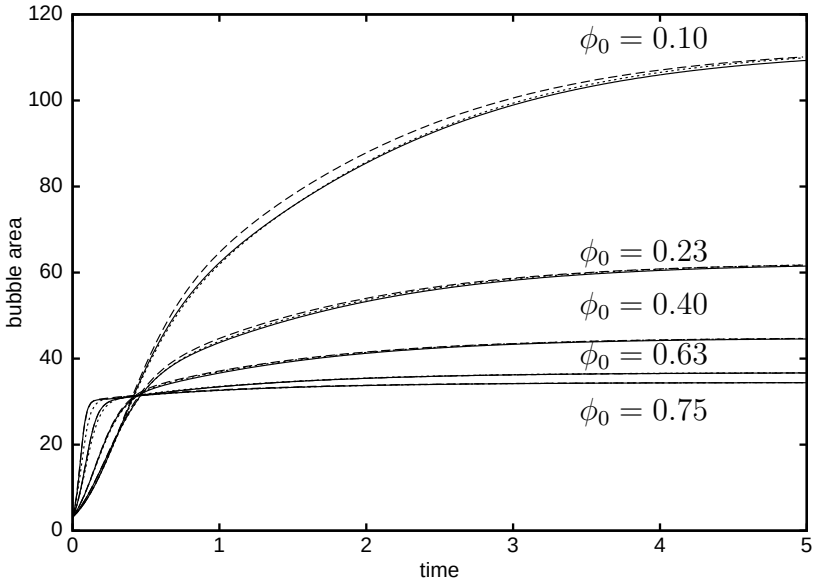

Fig. 9. Evolution of the bubble area for $De = 5$, $p_{g0} = 10p_a$, $\beta = 0.5$, $1/\Gamma = 0$ in the limit of infinite diffusivity. Solid line show results obtained from the full two-dimensional simulation; dashed line shows results from the thin approximation and the dotted line results from the circular approximation.

so that the total amount of gas in the system and hence the final bubble area is the same as the simulations for $N \to \infty$. Figure 8 shows the effect of diffusivity on bubble expansion for $\beta = 0.5$, $De = 10$, $\phi_0 = 0.630$ and $1/\Gamma = 0$. For $N \gg 1$ we recover the behaviour seen in figure 3 of a rapid initial expansion limited by viscosity followed by slower rate of expansion controlled by stress relaxation. At lower diffusivities the initial rate of expansion is limited by the availabity of gas to drive the expansion, however, even at $N = 0.1$ the expansion rate is still sufficiently rapid to stretch the polymers so that for $t > 1$ the expansion follows the behaviour for $N \gg 1$. For very small diffusivities $N \ll 1$ the diffusion limited expansion rate is too small to stretch the polymers and the bubble growth is the same as for a Newtonian fluid with equal zero-shear-rate viscosity.

The effect of initial bubble area fraction on its subsequent expansion is shown in figure 9. Here we show the evolution of the bubble area for different ϕ_0 in the range 0.1–0.75 with $p_{g0} = 10p_a$, $De = 5$, $\beta = 0.5$, $N \to \infty$ and $1/\Gamma = 0$. Since gas is transported from the fluid into the bubble during the ratio of the final to initial bubble radii, R_f/R_0, is given by

$$\frac{R_f}{R_0} = \sqrt{\left[\frac{p_{g0}\phi_0 + \Phi(p_{g0} - p_a)(1-\phi_0)}{\phi_0 p_a} + \left(\frac{p_{g0} - p_a}{2p_a De\Gamma}\right)^2\right]} - \frac{p_{g0} - p_a}{2p_a De\Gamma},$$

which decreases with increasing ϕ_0 for large $De\Gamma$. For the two smallest values of ϕ_0, 0.1 and 0.23 the initial growth is the same as for a bubble in an infinite fluid, however as ϕ_0 is increased the bubbles expand more rapidly since the

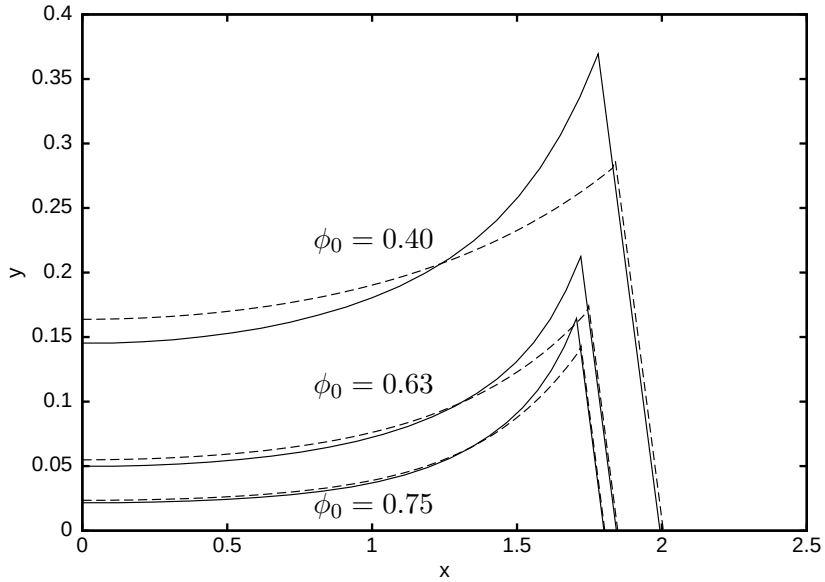

Fig. 10. Comparison of the shape of the bubble-liquid interface at $t = 1$ between the full two-dimensional simulation (solid line) and the thin-film approximation (dashed line) for the three largest values of ϕ_0 shown in figure 9.

resisting fluid layer is thinner. However, the bubbles grow to a smaller size due to the lower amount of gas in the system. Also shown on figure 9 are the bubble areas predicted by the two one dimensional approximations. As expected the circular approximation is most accurate for small area fractions. However, the bubble area evolution is predicted quite accurately for all values of ϕ_0 shown. Conversely the thin film approximation is most accurate at high area fractions, but again the preditions of bubble area growth are accurate for ϕ_0 as low as 0.23.

In figure 10 we compare the shape of the bubble between the full simulation and the thin-film approximation at $t = 1$ for the three largest values of ϕ_0 in figure 9. The thin-film model reproduces qualitatively the behaviour seen with the full calculations including the elastic recoil behaviour. However, for $\phi_0 < 0.63$ it underestimates the difference in thickness between the thinnest and thickest parts of the film. Unlike the full two-dimensional calculations, this one-dimensional theory does not impose the $\pi/3$ tangent to the bubble surface at the point C where the free surface meets the edge of the next image. Consequently it appears easier to draw fluid out of the strut than is true in practice.

At small area fractions and large surface tension the bubbles remain circular. Figure 11 shows the evolution of the maximum and minimum bubble radius obtained from the full two-dimensional calculations compared to the radius predicted by the circular approximation. In these simulations we include the effects of surface tension by setting $\Gamma = 1$, while other parameters are the same as those used in the simulations in figure 9. We find that the bubbles remain

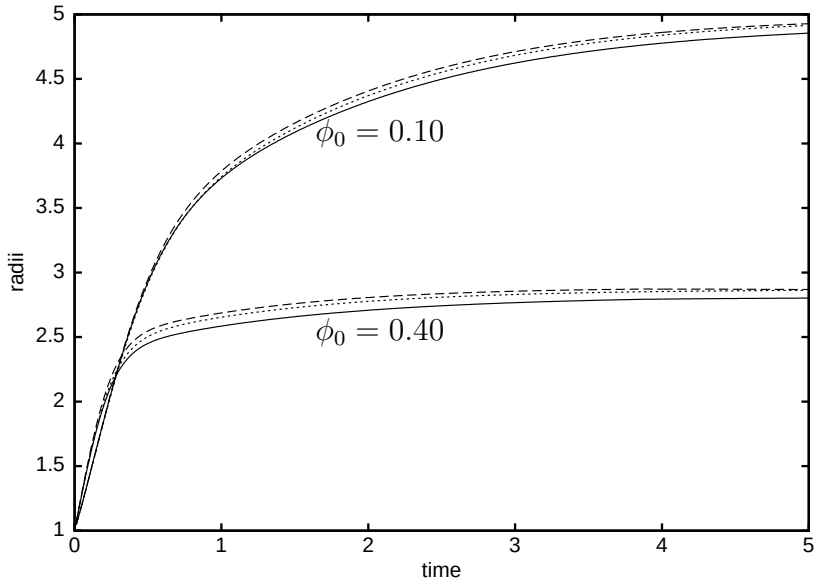

Fig. 11. Evolution of the minimum (solid line) and maximum (dashed line) bubble radii for $De = 5$, $p_{g0} = 10p_a$, $\beta = 0.5$ and $\Gamma = 1$ for $N \to \infty$. Dotted line show results from circular approximation.

approximately circular until their area fraction reaches 0.5 and that the radius predicted by the circular approximation is always between the maximum and minimum radius.

5 Bubbles expanding in a pompom fluid

The phenomena described in previous section arise from the extensional strain hardening of the Oldroyd B fluid. In a rapid extensional flow (*i.e.* $|\nabla \mathbf{u}|\tau > 1/2$) the extensional stress grows exponentially without bound. In the bubble expansion problem the strain experienced by a fluid element is limited by the supply of gas to Hencky strains of no more than 1.6. Thus for dilute solutions of large molecular weight polymers this is far below the strains required to see the effects of finite extensibility. However, more concentrated solutions and melts show much weaker strain-hardening. In this section we explore how the results in the previous section are affected by changing the constitutive model to one in which there is an upper limit on the extensional stress provided by the polymer.

We will use the differential version of the original pompom model [16], but with the modification introduced by Blackwell *et al* [6]. The model is obtained by considering a melt of 'pompom' molecules formed by connecting two q-armed star polymers with a backbone chain. The presence of the branch points at the ends of the backbone chain inhibits its motion along its tube, so that stretch and orientation relaxation times of the the backbone, τ_s and τ respectively, are

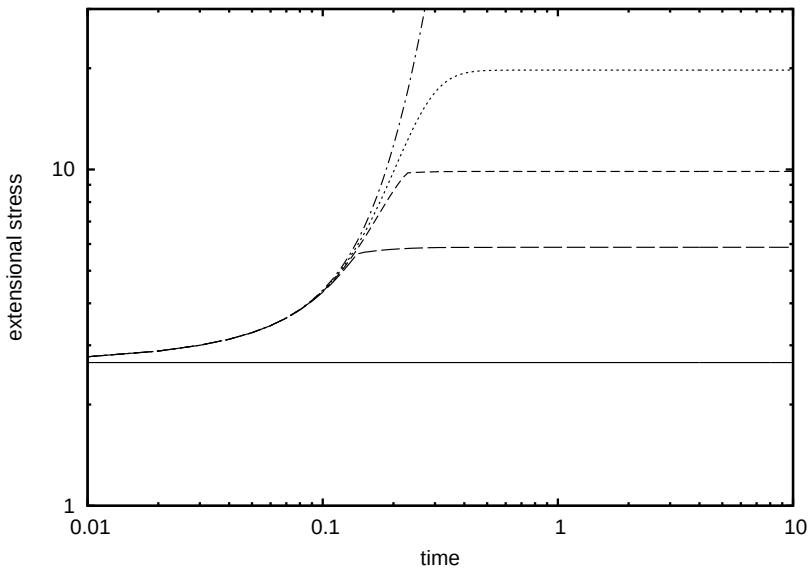

Fig. 12. Transient extensional difference $\sigma_{xx} - \sigma_{yy}$ for different values of q for $De_s = 10$, $De = 30$ and $\beta = 0.8$: solid line: solvent only; long-dashed line: $q = 2$; short-dashed line: $q = 3$; dotted line: $q = 5$; dash-dotted line $q = \infty$.

controlled by the relaxation of the star arms. The backbone chain segments will become extended by an extensional flow with velocity gradient, $|\nabla \mathbf{u}| > 1/\tau_s$. However, once the extension in the backbone becomes equal to q, part of the star arms are withdrawn into the backbone tube, thereby reducing the stretch relaxation time to balance the imposed extension rate. The effect is to limit polymer contribution to the extensional stress to $3Gq^2$, where G is the elastic modulus.

In order to facilitate comparison with our Oldroyd B calculations we shall consider a single pompom mode together with a solvent term so that equation (2) is replaced by

$$\boldsymbol{\sigma} = 2\mu\mathbf{E} + 3G\lambda^2 \frac{\mathbf{A}}{\mathrm{Tr}(\mathbf{A})}.$$

The tensor $\mathbf{A}$ remains given by equation (1) where τ is now the the orientation relaxation time, while the backbone stretch, λ, is given by

$$\frac{D\lambda}{Dt} = \frac{\lambda}{\mathrm{Tr}\mathbf{A}}\mathbf{A} : \nabla u - \frac{e^{2(\lambda-1)/q}}{\tau_s}(\lambda - 1), \tag{29}$$

up to the maximum stretch, q. We use same non-dimensionalisation used for the Oldroyd B model, so that the Deborah number is based upon the orientation relaxation time, τ. As well as the dimensionless groups listed in table 1, we now have two additional dimensionless groups: q, the number of arms and $De_s = De\tau_s/\tau$, the Deborah number based upon the stretch relaxation time.

In figure 12 we show the transient stress difference for the pompom model during start up of planar extensional flow for diffent values of q at $De = 30$,

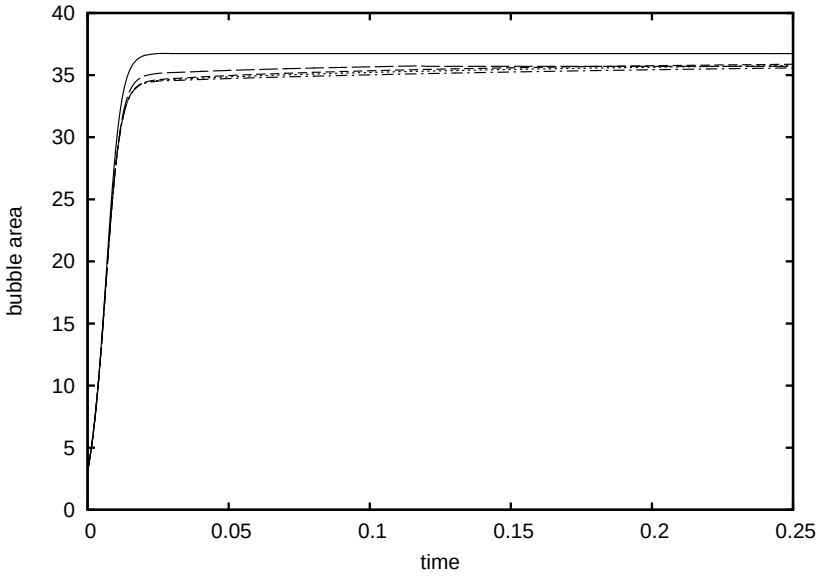

Fig. 13. The effect of the arm number, q, in the pompom model on the evolution of the bubble area for $De_s = 10$, $De = 30$, $p_{g0} = 10p_a$, $\beta = 0.8$ and $\phi_0 = 0.630$: solid line: solvent only; long-dashed line: $q = 2$; short-dashed line: $q = 3$; dotted line: $q = 5$; dash-dotted line $q = \infty$.

$\beta = 0.8$ and $\tau_s = \tau/3$, so that stretch Deborah number, $De_s = 10$. As $De_s \gg 1$, the stress rises grows exponentially with time until reaching its plateau value of $4(1-\beta)De+3\beta q^2$. Thus by varying q we can control the degree of extension hardening of the fluid.

Figure 13 shows the evolution of bubble area for the pompom model at different values of q for $\beta = 0.8$. The parameter values are the same as for figure 3, *i.e.* $\phi_0 = 0.63$ and $p_{g0} = 10p_a$, except that we have chosen to make the stretch Deborah $De_s = 10$ rather than the Deborah number based on orientation relaxation time, as it is the stretching rather than the orientation of backbones that contributes to the viscoelastic stress. The solid line in figure 13 shows the bubbble expansion for the case of pure solvent. As expected the bubble area is smaller for higher values of q, but what is somewhat surprising is that the differences between the different values of q are so small. This demonstrates that the evolution of bubble area is not particularly sensitive to the degree of strain-hardening provided the polymer is strain-hardening for small strains.

However, when we examine the evolution of the minimum thickness, AD, shown in figure 14 we find a marked difference between small and large values of q. For large values of q we see the minimum or 'bounce' in thickness found earlier with the Oldroyd model as the highly stretched fluid in the centre relaxes by pulling fluid in from the corners. However, for small values of q we see the opposite behaviour. Fluid is now drawn away from the thinnest part of the window, so that it becomes thinner even than the case of pure solvent. Thus in contrast to the case of the Oldroyd B fluid the polymer stresses produce a

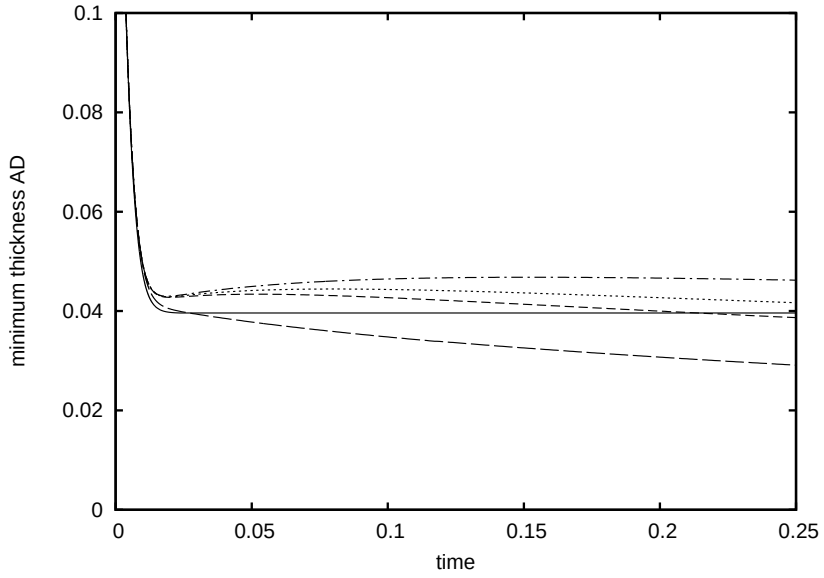

Fig. 14. The variation in the minimum thickness, AD, for different values of the arm number, q, for $De_s = 10$, $De = 30$, $p_{g0} = 10p_a$, $\beta = 0.8$ and $\phi_0 = 0.630$: solid line: solvent only; long-dashed line: $q = 2$; short-dashed line: $q = 3$; dotted line: $q = 5$; dash-dotted line $q = \infty$.

window that is less uniform in thickness.

For the pompom model equation (27) is replaced by

$$-4\frac{d\Delta y}{dt} + 3\beta\lambda^2(S_{xx} - S_{yy})\Delta y = F(t) \tag{30}$$

where $\mathbf{S} = \mathbf{A}/\mathrm{Tr}(\mathbf{A})$ is the orientation tensor. Thus the polymer contribution is limited to at most $3\beta q^2\Delta y$. Consequently in regions of the window where λ has stretched to its maximum value, the polymer contribution is proportional to Δy, so that the thicker regions will expand at the expense of the thinner regions.

Although we have only examined the pompom model, this phenomenon will occur in any viscoelastic model for which the polymeric extensional force (per unit length) $(\sigma_{xx} - \sigma_{yy})\Delta y$ decreases with increasing strain — the planar extensional analogue of the Considère condition discussed by McKinley and Hassager [15].

6 Axisymmetric Models

The foam structures in this paper are constructed from two-dimensional rather than three-dimensional bubble arrays and there are important geometric differences between expansion in two and three dimensions. However, the thin-

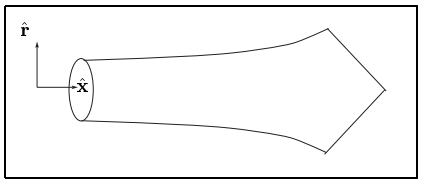

Fig. 15. Diagram showing the axisymmetric model for a strut in an open cell foam.

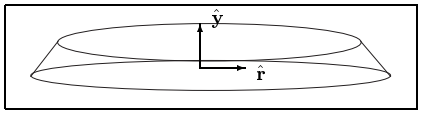

Fig. 16. Diagram showing the axisymmetric model for a circularly symmetric section of window between two neighbouring bubbles.

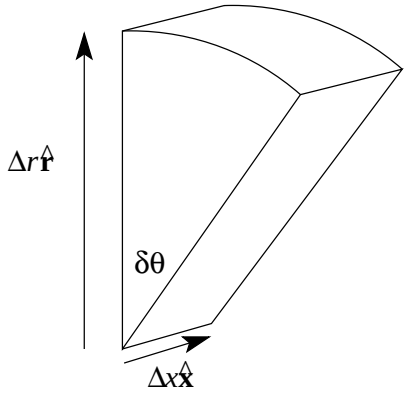

Fig. 17. Diagram showing the wedge shaped section of a fluid element.

film model can be extended to two axisymmetric problems that model the expansion of struts and windows in three dimensions. In the first, the axis of symmetry is AB giving a geometry that represents a strut in an open cell foam (figure 15). In the second, the axis of symmetry is AD giving a geometry that represents a circularly symmetric section of the window between two bubbles (figure 16).

6.1 Strut in an Open Cell Foam

The arguments of section 3.4 may be followed in the axisymmetric case by integrating the axial force over the surface of a wedge shaped fluid element as shown in figure 17. The curvature on the liquid-gas interface now has two terms. In addition to the longitudinal curvature there is a second term from the azimuthal curvature, giving

$$\kappa = \frac{\Delta r''}{(1+\Delta r'^2)^{3/2}} - \frac{1}{\Delta r(1+\Delta r'^2)^{1/2}} = -\frac{1}{\Delta r \Delta r'}\frac{d}{dx}\left(\frac{\Delta r}{(1+\Delta r'^2)^{1/2}}\right).$$

Combining the $\hat{\mathbf{x}}$ components gives the following non-dimensional force balance on each fluid element, equivalent to equation (20)

$$\Psi_{i+1} = \Psi_i - \frac{1}{\Gamma}\left(\frac{\Delta r_{i+1}}{(1+\Delta r'^2_{i+1})^{1/2}} + \frac{\Delta r''_{i+1}\Delta r^2_{i+1}}{(1+\Delta r'^2_{i+1})^{3/2}} - \frac{\Delta r_i}{(1+\Delta r'^2_i)^{1/2}} - \frac{\Delta r''_i \Delta r^2_i}{(1+\Delta r'^2_i)^{3/2}}\right) \quad (31)$$

where $\Psi = (\sigma_{xx} - \sigma_{rr})\Delta r^2$.

In order to link the extension of the strut to the volume expansion of the foam we must define an effective cell volume associated with this section of strut. One way to do this is to regard the strut section as half of an edge in a space filling regular truncated octahedron (or plane-faced isotropic tetrakaidecahedron) that is the straight-edged approximation to Kelvin's cell. This definition gives a cell volume of $8\sqrt{2}L^3/3$, where L is the length of the strut so that the effective bubble volume fraction $\phi = 1-3\sqrt{2}V_f/(16L^3)$ where V_f is the volume of fluid in the strut. Although this geometry represents a strut in an open cell foam we assume that there is a 'skin' round the outside of the foam so that gas pressure is prevented from leaking away allowing it to drive the expansion. Using equation (7) the pressure difference, P_g, is related to the stress in the liquid by

$$\frac{\pi}{6}\sum_i \left\{(\sigma_{xx}-\sigma_{rr})_{i+1} + (\sigma_{xx}-\sigma_{rr})_i\right\} \frac{d\Delta x_i}{dt}\left(\Delta r^2_{i+1} + \Delta r_{i+1}\Delta r_i + \Delta r^2_i\right) = 8\sqrt{2}P_g De L^2 \frac{dL}{dt} - \frac{1}{\Gamma}\sum_i \frac{dC_i}{dt}, \quad (32)$$

where C_i is now the surface area of the gas-liquid interface of element i. Conservation of fluid volume gives

$$\frac{1}{\Delta x}\frac{d\Delta x}{dt} = -\frac{\frac{d\Delta r_{i+1}}{dt}(2\Delta r_{i+1} + \Delta r_i) + \frac{d\Delta r_i}{dt}(\Delta r_{i+1} + 2\Delta r_i)}{\Delta r^2_{i+1} + \Delta r_{i+1}\Delta r_i + 2\Delta r^2_i}, \quad (33)$$

and the gas pressure is given by,

$$(p_{g0} - p_a)P_g = p_{g0}\left(\frac{8\sqrt{2}{L_0}^3 - 3V_f(1-\Phi)}{8\sqrt{2}L^3 - 3V_f(1-\Phi)}\right) - p_a. \quad (34)$$

In the Oldroyd B model,

$$\sigma_{xx} - \sigma_{rr} = -\frac{3}{\Delta r}\frac{d\Delta r}{dt} + \beta(A_{xx} - A_{rr})$$

where the evolution of $\mathbf{A}$ is given by

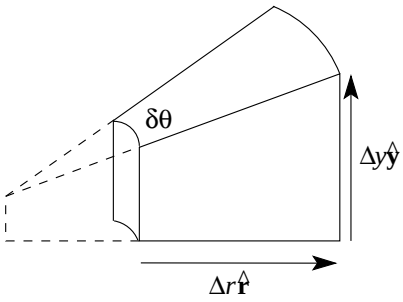

Fig. 18. Diagram showing the section of fluid element used to obtain a force balance.

$$\frac{dA_{rr}}{dt} = \frac{2}{\Delta r}\frac{d\Delta r}{dt}A_{rr} - (A_{rr} - 1) \tag{35}$$

$$\frac{d}{dt}(A_{rr} - A_{xx}) = -\frac{4}{\Delta r}\frac{d\Delta r}{dt}(A_{rr} - A_{xx}) + 3A_{rr}) - (A_{rr} - A_{xx}). \tag{36}$$

6.2 Circularly Symmetric Section of the Window Between Two Bubbles

For the second axisymmetric case we integrate the momentum equation, using the divergence theorem, round the surface of the section of fluid element shown in figure 18. This leads to the following force balance

$$\Psi_{i+1}r_{i+1} = \Psi_i r_i + \frac{(r_{i+1} - r_i)}{2}(\Theta_i + \Theta_{i+1}) - \frac{1}{2\Gamma}(\kappa_{i+1} - \kappa_i)(r_i\Delta y_{i+1} + r_{i+1}\Delta y_i) \tag{37}$$

where $\Psi = (\sigma_{rr} - \sigma_{yy})\Delta y$ and $\Theta = \sigma_{\theta\theta}\Delta y$. There are, again, two curvature terms contributing to the surface tension, giving

$$\kappa = \frac{\Delta y''}{(1 + \Delta y'^2)^{3/2}} + \frac{\Delta y'}{r(1 + \Delta y'^2)^{1/2}}.$$

Once again we use the truncated octahedron to define an effective cell volume based on its ratio of volume squared to surface area cubed. With this definition the effective cell volume, V_c, is given by

$$V_c = \left(\frac{4\pi}{3 + 6\sqrt{3}}\right)^{3/2} L^3 = XL^3$$

where L is radius the of the circular window.

From equation (7) we obtain

$$\pi\sum_i (\Upsilon_{i+1} + \Upsilon_i)(r_{i+1} - r_i) = 3XP_gDeL^2\frac{dL}{dt} - \frac{1}{\Gamma}\sum_i \frac{dC_i}{dt}. \tag{38}$$

where

$$\Upsilon = (\sigma_{yy} - \sigma_{rr})r\frac{d\Delta y}{dt} + (\sigma_{\theta\theta} - \sigma_{rr})\Delta y\frac{dr}{dt}.$$

Gas pressure is obtained from mass conservation as

$$(p_{g0} - p_a)P_g = p_{g0}\left(\frac{XL_0{}^3 - V_f(1-\Phi)}{XL^3 - V_f(1-\Phi)}\right) - p_a. \tag{39}$$

In this geometry the volume of a fluid element is given by

$$r_{i+1}^2\Delta y_{i+1} - r_i^2\Delta y_i - \frac{1}{3}(r_{i+1}^2 + r_{i+1}r_i + r_i^2)(\Delta y_{i+1} - \Delta y_i)$$

and so conservation of volume gives,

$$\begin{aligned}\frac{dr_{i+1}}{dt}\left(2r_{i+1}\Delta y_{i+1} - \frac{1}{3}(2r_{i+1} + r_i)(\Delta y_{i+1} - \Delta y_i)\right)& \\ + \frac{1}{3}\frac{d\Delta y_{i+1}}{dt}\left(2r_{i+1}^2 - r_{i+1}r_i - r_i^2\right)& \\ = \frac{dr_i}{dt}\left(2r_i\Delta y_i + \frac{1}{3}(r_{i+1} + 2r_i)(\Delta y_{i+1} - \Delta y_i)\right)& \\ + \frac{1}{3}\frac{d\Delta y_i}{dt}\left(-r_{i+1}^2 - r_{i+1}r_i + 2r_i^2\right).&\end{aligned} \tag{40}$$

For the Oldroyd B fluid the stresses, σ_{rr}, σ_{yy} and $\sigma_{\theta\theta}$ are given by,

$$\sigma_{rr} = -\frac{2}{\Delta y}\frac{d\Delta y}{dt} - \frac{2}{r}\frac{dr}{dt} + \beta A_{rr}, \tag{41}$$

$$\sigma_{yy} = \frac{2}{\Delta y}\frac{d\Delta y}{dt} + \beta A_{yy}, \tag{42}$$

$$\sigma_{\theta\theta} = \frac{2}{r}\frac{dr}{dt} + \beta A_{\theta\theta} \tag{43}$$

together with the evolution equations

$$\frac{dA_{yy}}{dt} = \frac{2}{\Delta y}\frac{d\Delta y}{dt}A_{yy} - (A_{yy} - 1) \tag{44}$$

$$\frac{dA_{rr}}{dt} = -\left(\frac{2}{\Delta y}\frac{d\Delta y}{dt} + \frac{2}{r}\frac{dr}{dt}\right)A_{rr} - (A_{rr} - 1) \tag{45}$$

$$\frac{dA_{\theta\theta}}{dt} = \frac{2}{r}\frac{dr}{dt}A_{\theta\theta} - (A_{\theta\theta} - 1). \tag{46}$$

The method of solution is as described in section 3.4 for the thin-film approximation to planar flow.

6.2.1 Results For Axisymmetric Models

In the planar array the surface tension arising from the curvature of the bubble-liquid interface acts to restore circular bubbles and to limit the size of

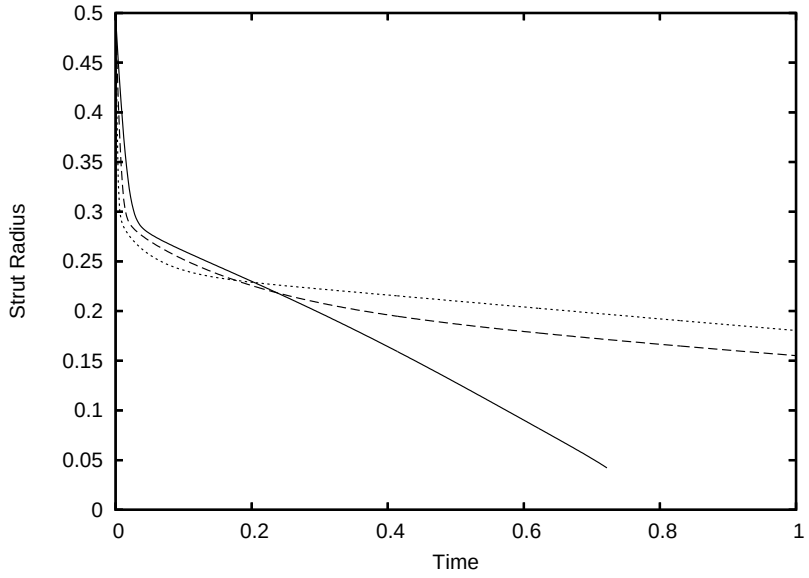

Fig. 19. Plot of the minimum strut radius as a function of time for $De = 10$, $p_{g0} = 10p_a$, $1/\Gamma = 5$ and $\phi_0 = 0.75$: solid line, $\beta = 0$ (Newtonian); dashed line, $\beta = 0.5$; dotted line, $\beta = 0.8$.

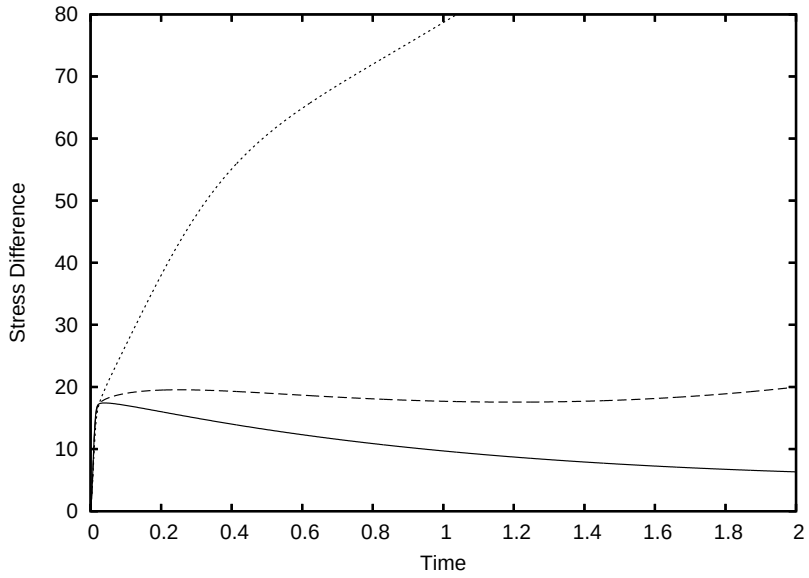

Fig. 20. Evolution of the polymer stretch difference $A_{xx} - A_{rr}$ for $De = 10$, $p_{g0} = 10p_a$, $\beta = 0.5$ and $\phi_0 = 0.75$: solid line, $1/\Gamma = 1$; dashed line: $1/\Gamma = 2$; dotted line, $1/\Gamma = 5$.

the bubble by modifying the bubble gas pressure. In the axisymmetric geometries the presence of the extra curvature adds a second surface tension term. In the case of the liquid strut it acts in the opposite direction, providing a capillary pressure proportional to $1/\Delta r$. As the strut extends this azimuthul curvature ultimately dominates and in a Newtonian fluid causes the minimum radius to decrease linearly in time until the breakage occurs. However, Entov and Hinch [7] show that a viscoelastic filament stretching due to capillary

pressure thins much more slowly than a Newtonian fluid due to the resistance provided by the polymers. The radius reduces exponentially at the (longest) relaxation rate and break-up only occurs in finite time due to the limited extensibility of the polymers in their FENE constitutive model.

Figure 19 shows the effect of viscoelasticity on the minimum radius of the strut. For high Deborah numbers and moderate capillary numbers the dynamics can be divided into three phases. First, we see the same rapid expansion driven by the gas pressure as in the planar case. The Newtonian strut thins more slowly during this phase due to its higher fluid viscosity. After this phase of bubble expansion the thinning of the strut is driven by capillary pressure. For moderate capillary numbers, ($1/\Gamma \leq 2$ in figure 20) the extension rate falls below the coil-stretch transition rate so that the polymers begin to relax. However, as the strut continues to thin the rate-of-extension increases so that the polymers become extended again. In the final phase the capillary pressure is resisted by the polymer stress, so that for $\beta > 0$ the minimum radius decreases exponentially. These last two phases are equivalent to the first two phases of filament stretching discussed by Entov and Hinch. We do not see their final phase of finite time break-up as our Oldroyd B model does not include finite extensibility.

In the circularly symmetric window section the axisymmetric curvature term is proportional to $\Delta y'/r$ and acts in the same sense as the surface tension associated with the interface, thus inhibiting bubble growth. The presence of the second surface tension term means that surface tension has a greater effect on reducing the bubble expansion for the same value of the capillary number. The effects of viscoelasticity are the same as for the planar case, since the Oldroyd B model has the same strain-hardening behaviour in biaxial, planar and uniaxial extension.

7 Conclusions

In this paper we have considered the effects of large gas volume fraction on the expansion of gas bubbles in a viscoelastic fluid. Initially the bubbles are effectively isolated, but as they expand the liquid surrounding them becomes stretched into thin films separating neighbouring bubbles. Our two-dimensional calculations capture this changing structure for planar bubbles in a hexagonal array. Although this is not the geometry found in real three-dimensional foams, the results of the previous section suggest that the effects of viscoelasticity are qualitatively similar between two and three dimensions.

Viscoelasticity controls the bubble growth when the gas diffusion is sufficiently rapid to allow the bubbles to expand at a rate faster than the polymer relax-

ation time. In this regime we see the same two stage expansion found previously for isolated spherical bubbles [9]. The bubbles initially grow rapidly until they reach a size where the elastic polymer stress balances the pressure difference. Beyond this time the bubbles continue to grow at the polymer relaxation rate as the stress relaxes. During the initial phase the polymers become most extended in the mid sections of the windows where the fluid layer is thinnest. Once stretched the polymers resist further extension and draw fluid back from the corners during the relaxation phase. The result is that polymeric foams have a more even thickness of fluid surrounding the gas bubbles than Newtonian foams, provided that the system is quenched before surface tension restores the interface to circular arcs. The extension hardening of the polymer acts to stabilise the fluid interfaces against breakage.

As well as the full two-dimensional calculation we also considered two one-dimensional approximations: a circular model valid at low gas area fractions and a thin film model valid at high gas area fractions. Both of these simplified models gave accurate predictions of the bubble area over a wide range of parameter values, suggesting that gas area is not particularly sensitive to the detailed flow in the films. This suggests that models of three dimensional foams that assume spherical symmetry should give accurate predictions of bubble volumes to quite high gas volume fractions. However, these approximate models only captured the detailed shape of the fluid films over a much more restricted range of parameters, although the thin film model does give the correct qualitative behaviour. Thus for high gas volume fractions three-dimensional foams could be investigated using an analogue of the thin film model to avoid having to compute the full three dimensional flow.

In this paper we have generally used the Oldroyd B fluid to model the polymeric fluid. Although this simple model reproduces the extension hardening characteristic of dilute polymer solutions it has several shortcomings. In particular it has a constant viscosity in shear and has infinite extensibility. However, these shortcomings are less important in the flow considered here. The flow is almost shear free and the extensions are limited by the growth of the bubble which is determined by the available supply of gas.

In order to determine the sensitivity of the results to the degree of strain-hardening, we replaced the Oldroyd B fluid with a 'pompom' fluid for different values of the extensibility parameter q. We find that while the predicted bubble area changes only slightly with q the shape of the interface is quite different. For fluids with limited strain-hardening (small values of q) the elastic stresses pull fluid away from the thinnest part of the window and so act to destabilise rather than stabilise the liquid films.

In this paper we have assumed that the bubbles are all identical and evenly spaced on a hexagonal array. In practice foams are disordered with a wide

range of bubble sizes. In foams with bubbles of different sizes neighbouring bubbles compete unevenly for the available gas. This effect will be considered in the next paper [8].

Acknowledgements

Sally Everitt would like to acknowledge the EPSRC and Huntsman Polyurethanes (an international business of Huntsman International LLC) for their financial support. We would also like to thank Tim Nicholson for the use of his flow visualisation software, FlowDis, and Don Jones for many useful discussions.

References

[1] M. Amon and C. Denson. A Study of the Dynamics of Foam Growth:Analysis of the Growth of Closely Spaced Spherical Bubbles. *Polymer Engineering and Science*, 24:1026–1034, Sept 1984.

[2] A Arefmanesh, S G Advani, and E E Michaelides. An accurate numerical solution for mass diffusion induced bubble growth in viscous liquids containing limited dissolved gas. *Int. J. Heat Mass Trans*, 35:1711–1722, 1992.

[3] A. Arefmanesh and S.G. Advani. Diffusion Induced Growth of a Gas Bubble in a Viscoelastic Fluid. *Rheologica Acta*, 30:274–283, 1991.

[4] A. Arefmanesh and S.G. Advani. Non-Isothermal Bubble Growth in Polymeric Foams. *Polymer Engineering and Science*, 35:252–260, February 1995.

[5] R.B. Bird, R.C. Armstrong, and O. Hassager. *Dynamics of Polymeric Fluids, Volume 1.* John Wiley and Sons, 1987.

[6] R. Blackwell, T.C.B. Mcleish, and O.G. Harlen. Molecular Drag-Strain Coupling in Branched Polymer Melts. *Journal of Rheology*, 44:121–136, Jan/Feb 2000.

[7] V.M. Entov and E.J. Hinch. Effect of a Spectrum of Relaxation Times on the Capillary Thinning of a Filament of Elastic Liquid. *Journal of Non-Newtonian Fluid Mechanics*, 72:31–53, 1997.

[8] S.L. Everitt, O.G. Harlen, and H.J. Wilson. Competition and interaction of polydisperse bubbles in reacting and non-reacting polymer foams. *Journal of Non-Newtonian Fluid Mechanics*, 2006. in press.

[9] S.L. Everitt, O.G. Harlen, H.J. Wilson, and D.J. Read. Bubble Dynamics in Reacting and Non-Reacting Polymer Foams. *Journal of Non-Newtonian Fluid Mechanics*, 114:83–107, 2003.

[10] M Favelukis. Dynamics of foam growth: Bubble growth in a limited amount of liquid. *Polymer Engg Sci.*, 44:1900–1906, 2004.

[11] R.J. Fisher and M.M. Denn. A Theory of Isothermal Melt Spinning and Draw Resonance. *AIChE Journal*, 22(2):236–246, March 1976.

[12] C.J. Han and H.J. Yoo. Studies on Structural Foam Filling. IV Bubble Growth During Mould Filling. *Polymer Engineering and Science*, 21:518–533, June 1981.

[13] O.G. Harlen, J.M. Rallison, and P. Szabo. A Split Lagrangian-Eulerian Method for Simulating Transient Viscoelastic Flows. *Journal of Non-Newtonian Fluid Mechanics*, 60:82–104, 1995.

[14] R.G. Larson. Analysis of Isothermal Fiber-Spinning With The Doi-Edwards Constitutive Model. *Journal of Rheology*, 27(5):475–496, 1983.

[15] G.H. McKinley and O. Hassager. The Considère condition and rapid stretching of linear and branched polymer melts. *Journal of Rheology*, 43(5):1195–1212, 1999.

[16] T.C.B. McLeish and R.G. Larson. Molecular Constitutive Equations for a class of branched polymers: The Pompom Polymer. *Journal of Rheology*, 42:81–110, 1998.

[17] C. Pozrikidis. Expansion of a Two-dimensional Foam. *Engineering Analysis with Boundary Elements*, 26:495–504, 2002.

[18] N S Ramesh and N Malwitz. A non-isothermal model to study the influence of blowing agent concentration on polymer viscosity and gas diffusivity in thermoplastic foam extrusion. *J. Cell. Plas.*, 35:199–209, 1999.

[19] N.S. Ramesh, D.H. Rasmussen, and G.A. Campbell. Numerical and Experimental Studies of Bubble Growth During the Microcellular Foaming Process. *Polymer Engineering and Science*, 31:1657–1664, December 1991.

[20] L.W. Schwartz and R.V. Roy. Interim Report: Theoretical and Numerical Modelling of an Expanding Foam. Technical report, University of Delaware, Newark, Delaware, USA, January 2000.

[21] M.A. Shafi and R.W. Flumerfelt. Initial Bubble Growth in Polymer Foam Processes. *Chemical Engineering Science*, 52:627–633, 1997.

[22] M.A. Shafi, K. Joshi, and R.W. Flumerfelt. Bubble Size Distribution in Freely Expanded Polymer Foams. *Chemical Engineering Science*, 52:635–644, 1997.

[23] J.R. Street. The Rheology of Phase Growth in Elastic Liquids. *Transactions of the Society of Rheology*, 12:103–131, 1968.

[24] I. Tanasawa and W. Yang. Dynamic Behavior of a Gas Bubble in Viscoelastic Fluids. *Journal of Applied Physics*, 41:4526–4531, October 1970.

[25] R. Ting. Viscoelastic Effect of Polymers on Single Bubble Dynamics. *AIChE Journal*, 21:810–813, July 1975.

[26] D. Vaynblat, J.R. Lister, and T.P. Witelski. Rupture of Thin Viscous Films by Van der Waals Forces: Evolution and Self-similarity. *Physics of Fluids*, 13(5):1130–1140, May 2001.

[27] DC Venerus, N Yala, and Bernstein B. Analysis of diffusion-induced bubble growth in viscoelastic liquids. *J. Non-Newtonian Fluid Mech.*, 75:55–75, 1998.

[28] W.W. Zhang and J.R. Lister. Similarity Solutions for Van der Waals Rupture of a Thin Film on a Solid substrate. *Physics of Fluids*, 11(9):2454–2462, September 1999.